Numerical Evaluations of the Effect of Feature Maps on Content-Adaptive Finite Element Mesh Generation

W. H. Lee, T.-S. Kim, M. H. Cho, S. Y. Lee

Functional and Metabolic Imaging Center
Department of Biomedical Engineering Kyung Hee University
Yongin, Gyeonggi, Republic of Korea
(Received November 16, 2006. Accepted December 12, 2006)

Abstract

Finite element analysis (FEA) is an effective means for the analysis of bioelectromagnetism. It has been successfully applied to various problems over conventional methods such as boundary element analysis and finite difference analysis. However, its utilization has been limited due to the overwhelming computational load despite of its analytical power. We have previously developed a novel mesh generation scheme that produces FE meshes that are content-adaptive to given MR images. MRI content-adaptive FE meshes (cMeshes) represent the electrically conducting domain more effectively with far less number of nodes and elements, thus lessen the computational load. In general, the cMesh generation is affected by the quality of feature maps derived from MRI. In this study, we have tested various feature maps created based on the improved differential geometry measures for more effective cMesh head models. As performance indices, correlation coefficient (CC), root mean squared error (RMSE), relative error (RE), and the quality of cMesh triangle elements are used. The results show that there is a significant variation according to the characteristics of specific feature maps on cMesh generation, and offer additional choices of feature maps to yield more effective and efficient generation of cMeshes. We believe that cMeshes with specific and improved feature map generation schemes should be useful in the FEA of bioelectromagnetic problems.

Key words : finite element analysis, MRI, content-adaptive mesh generation

I. INTRODUCTION

In solving bioelectromagnetic problems, the finite element analysis (FEA) is the most widely used method which offers a numerical and computational technique to obtain approximate solutions of the partial differential equations (PDEs). The use of FEA is significantly increasing in various fields such as biomechanics, bioelectromagnetics, and biomolecular imaging, since FEA offers a powerful analytical means in dealing with bioelectromagnetic phenomenon effectively. Moreover, the applications of FEA have become more popular in the biomedical fields such as biomechanical analysis [1] and biomedical imaging [2, 3]. The FE method allows (i) incorporation of anisotropic electrical properties of tissues, (ii) representation of arbitrary head geometry with complicated boundaries, and (iii) realistically volumetric analysis with numerical and computing power. For instance, Marin et al reported the influence of skull anisotropy on the forward and inverse solutions in EEG using realistic head models [4]. The influence of anisotropic conductivity tensors on the scalp electrical potentials and EEG distributed source imaging with 2-D FE head models also were investigated in [5] and [6].

To apply the FEA to bioelectromagnetic problems, the first and major requirement is the mesh generation of an electrically conducting volume. Numerical attempts to develop effective and efficient mesh generation methods for complex volumes were presented such as in [7] and [8]. In addition, several commercial packages offer a tool of generating uniform meshes to represent a complex volume such as COMSOL [9] and Nastran [10]. However, one major limitation in applying the FE method over conventional methods such as boundary element method and finite difference method is overly created number of nodes and elements, which result in the overwhelming computational

This study was supported by a grant of the Korea Health 21 R&D Project, Ministry of Health and Welfare, Republic of Korea (02-PJ3-PG6-EV07-0002).
Corresponding Author : Tae-Seong Kim, Ph.D.
Functional and Metabolic Imaging Center Department of Biomedical Engineering Kyung Hee University 1 Seocheon-dong, Giheung-gu, Yongin-si, Gyeonggi-do, Republic of Korea, 446-701
Tel : +82-31-201-3731 / Fax : +82-31-201-3666
E-mail : tskim@khu.ac.kr

load.

One of the ways to decrease the computational load is to reduce node and element numbers, while maintaining its numerical accuracy of FEA, which could be an outstanding benefit to FEA applications. Mesh refinement technique is one of the common methods for such purpose by representing the region of interest with much smaller elements [11, 12, 13].

Recently, we have developed a novel mesh generation scheme that produces FE meshes that are content-adaptive to given MR images or volumes of different geometries from individuals [14]. One advantage of these content-adaptive FE meshes (cMeshes) is the representation of the complex domain using optimal number of nodes and elements. We have demonstrated that the same computing domain could be represented with far less node and element numbers. Also we have shown the numerical evaluations of these cMeshes with a significant gain in computation time via EEG forward solutions to test their effectiveness with 3-D cMesh models. The detailed methodology of generating cMeshes is given in [14]. In this work, we have tested the effects of various feature maps derived from given MR image on the cMesh generation. To test the effects of feature maps, we have generated various feature maps by incorporating two advanced methods offering additional choices. First, we generated tensor-driven feature extractors derived from the eigenvalues of the Hessian and Structure tensor. Second, we utilized the principal curvature schemes including the Mean and Gaussian curvature to develop more effective feature maps. Also we have evaluated the effectiveness on our cMesh FE head models generated by each and specific feature map.

In this paper, we have studied how various feature maps affect the accuracy and efficiency of cMesh generation techniques. For such purpose, we generate several specific feature maps, and then evaluate the content-adaptiveness of cMeshes and the quality of cMesh triangle elements. The paper first introduces the conventional mesh generation schemes in Section A. In the following section, we introduce the procedures of how to generate cMeshes from MR image. In Section C, the methods of how to extract feature maps are demonstrated. This section continues to describe conventional and advanced feature map generation techniques based on the improved differential geometry measures. In Section D, numerical evaluations are demonstrated to investigate the content-adaptiveness of cMeshes and the quality of cMesh triangle elements from the conventional and proposed approaches. In the following, the results of feature map extraction, cMesh generation, comparisons, and numerical evaluations are given. Finally the paper is concluded with remarks on future works.

II. METHODS

A. Conventional Mesh Generation Schemes

Most mesh generation schemes used for bioelectromagnetic problems can be categorized into two parts. The first is uniform mesh generation in which FEs of approximately same size are generated to represent a complex volume. Examples can be found in the works of [5], [6], and [15]. The second technique by Ziolkowski and Brauer [13] used a local mesh refinement technique, but required user's guidelines to select local areas and used FEs. Although the procedure for these mesh generations is easy and straightforward, one of the critical shortcomings of these mesh generation schemes is the overly produced FEs, thus demanding the overwhelming computational load.

B. Content-adaptive Mesh Generation

Our content-adaptive mesh generation scheme [14] consists of the following steps: namely (i) generation of a feature map reflecting the spatial distributions of the structural informaiton of given image, (ii) node sampling from the feature map using a digital halftoning technique, and (iii) mesh generation via Delaunay tessellation. The cMesh generation relies on the performance of two key techniques: the quality of feature maps and the accuracy of content-adaptive node sampling. In this work, we focus on the former and its effects on cMeshes to generate more efficient and accurate cMesh FE models.

C. Image Feature Map Generation

To generate new and improved feature maps from given MRI, we have used tensor-driven methods using Hessian [8, 16], Structure tensor [17], and principal curvature methods such as Mean and Gaussian curvature [18, 19].

Conventional Feature Map Generation

In the work of Yang *et al* [8], two types of feature map generation techniques were proposed from a Hessian tensor of each pixel, H:

$$\mathbf{H} = \begin{bmatrix} I(i,j)_{xx} & I(i,j)_{xy} \\ I(i,j)_{yx} & I(i,j)_{yy} \end{bmatrix} \quad (1)$$

where I is an image, i and j are image indices, x and y indicate partial derivates in space. One feature map was derived from the maximum of Hessian tensor components:

$$f_{\max}(i,j) = \max\{|I_{xx}(i,j)|, |I_{xy}(i,j)|, |I_{yy}(i,j)|\} \quad (2)$$

Another suggested feature map was derived from the eigenvalues, μ's, of the tensor:

$$f_{H\max}(i,j) = \max\{|\mu_1(i,j)|, |\mu_2(i,j)|\} \quad (3)$$

The two eigenvalues of the Hessian matrix, denoted by μ_1 and μ_2 are given by

$$\mu_1 = \frac{1}{2}\left[(I_{xx}+I_{yy}) + \sqrt{(I_{xx}-I_{yy})^2 + 4I_{xy}^2}\right] \quad (4)$$

$$\mu_2 = \frac{1}{2}\left[(I_{xx}+I_{yy}) - \sqrt{(I_{xx}-I_{yy})^2 + 4I_{xy}^2}\right] \quad (5)$$

The Hessian tensor approach was utilized to extract image feature information from given MRI, since one critical attribute of its ability is highly sensitive toward feature orientations with the second-order directional derivatives. However, it is known to be highly sensitive toward noise as well.

Advanced Feature Map Generation

The conventional feature maps proposed by Yang *et al* [8] showed the adequate procedures for the purpose of image representation that cMeshes are adaptive to the contents of an image. Currently, improved differential geometry provides better choices in deriving feature maps with more effective and accurate properties. In this study, we have derived advanced feature maps based on the Hessian and Structure tensor as alternative ways [14].

For the Hessian approach, we have derived the feature maps with the eigenvalues of the tensor in the following way

$$f_{\mathbf{H}+}(i,j) = \sqrt{(\mu_1^{\mathbf{H}}(i,j) + \mu_2^{\mathbf{H}}(i,j))} \quad (6)$$

$$f_{\mathbf{H}}(i,j) = \sqrt{(\mu_1^{\mathbf{H}}(i,j)} \quad (7)$$

$$f_{\mathbf{H}-}(i,j) = \sqrt{(\mu_1^{\mathbf{H}}(i,j) - \mu_2^{\mathbf{H}}(i,j))} \quad (8)$$

where μ's are the positive eigenvalues of the tensor matrix.

Another proposed approach is the utilization of the Structure tensor due to robustness in detecting fundamental features of objects. The Structure tensor S can be expressed as follows:

$$\mathbf{S} = \begin{bmatrix} I_x^2 & I_x I_y \\ I_y I_x & I_y^2 \end{bmatrix} \quad (9)$$

We have derived new feature maps again with the eigenvalues of the Structure tensor as the same ways of the Hessian tensor:

$$f_{\mathbf{S}+}(i,j) = \sqrt{(\mu_1^{\mathbf{S}}(i,j) + \mu_2^{\mathbf{S}}(i,j))} \quad (10)$$

$$f_{\mathbf{S}}(i,j) = \sqrt{(\mu_1^{\mathbf{S}}(i,j)} \quad (11)$$

$$f_{\mathbf{S}-}(i,j) = \sqrt{(\mu_1^{\mathbf{S}}(i,j) - \mu_2^{\mathbf{S}}(i,j))} \quad (12)$$

The above feature map reflects the edges and corners of image structures for the plus sign. By taking the maximum eigenvalue, new feature map can be derived which is a natural extension of the scalar gradient viewed as the value of maximum variations. The other feature map represents the local coherence or anisotropy for the minus sign [20].

Also we have generated new feature maps via the principal curvature. There are geometric meanings with respect to the eigenvalues and eigenvectors of the tensor matrix. The first eigenvector (corresponding eigenvalue represents the largest absolute values) is the direction of greatest curvature. Conversely, the second eigenvector is the direction of least curvature. Also its eigenvalue has the smallest absolute value. The consistent eigenvalues are the respective amounts of these curvatures. The eigenvalues of tensor matrix with real values indicate principal curvatures, and are invariant under rotation.

The Mean curvature [18, 19] can be obtained from the Hessian tensor matrix. It is equal to the half of the trace of H which is invariant to the selection of x and y as well. The new feature map via the Mean curvature can be expressed as follows:

$$f_M(i,j) = \frac{I_{xx}(1+I_y^2) - 2I_x I_y I_{xy} + I_{xy}(1+I_x^2)}{2(1+I_x^2+I_y^2)^{3/2}} \quad (13)$$

From the Hessian tensor again, we can also derive new feature map by using the Gaussian curvature as shown below:

$$f_G(i,j) = \frac{I_{xx}I_{yy} - I_{xy}^2}{(1+I_x^2+I_y^2)^2} \quad (14)$$

D. Numerical Evaluations of cMeshes

Evaluations of Content-adaptiveness of cMeshes

In order to compare the effects of the feature maps on cMeshes, we have used the following five indices as the goodness measures of content-adaptiveness: (i) correlation coefficient (CC) of the feature map to the original MRI, (ii) root mean squared error (RMSE), (iii) residual error (RE) between the original MRI and the reconstructed MRI based on the nodal MR intensity values, (iv) number of nodes, and (v) number of elements. For the fair comparison of the cMesh qualities, almost same number of nodes and elements were generated by adjusting the mesh parameter. The total number of content-adaptive nodes is controlled by adjusting the parameter, as shown below.

$$f'(i,j) = f(i,j)^{1/\kappa} \tag{15}$$

where f is a feature map and k is a control parameter for the number of content-adaptive nodes.

In order to check the content information of the nonuniformly spaced nodes, the MR images were reconstructed only using the MR intensity values at the sampled nodes via cubic interpolation. Then the RMSE and RE values were computed between the original and the reconstructed MRI.

Evaluations of cMesh Quality

The mesh quality highly affects computational analysis in terms of numerical accuracy of the solution on FEA. The evaluation of mesh quality is highly critical, since it provides some indications and insights of how appropriate a particular discretization is for the numerical accuracy on FEA.

For a triangle element, the mesh quality measure can be expressed as

$$q = \alpha \frac{A}{l_1^2 + l_2^2 + l_3^2} \tag{16}$$

where A represents the area of the triangle, and l_1, l_2, and l_3 are the side lengths of the triangle elements, and $\alpha = 4\sqrt{3}$ is a normalizing coefficient justifying the quality of an equilateral triangle to 1 (i.e., q=1, when $l_1 = l_2 = l_3$. If q>0.6, the triangle possesses acceptable mesh quality [21]). The overall mesh quality was evaluated for triangular elements in terms of the arithmetic mean by

$$Q_a = \frac{1}{N}\sum_{i=1}^{N} q_i \tag{17}$$

where N indicates the number of elements. The mean value as the overall mesh quality indicator is highly sensitive to the occurrence of elements with an extremely "poor" mesh quality of triangle elements. Also it represents the worst mesh quality and the distribution of mesh quality. Certainly, other measures are available such as examination of dihedral angles of the triangle elements and other geometric measures [22, 23].

III. RESULTS

A. MRI Preprocessing

A single MR slice was selected from a set of multi-slice anatomical MR images covering the whole head which was obtained from 3.0T MRI scanner (Magnum 3.0, Medinus Inc., Korea) via a standard anatomical MR imaging sequence with the following scan parameters: 128 transaxial slices, TR= 35ms, TE=7ms, and slice thickness=2mm. Morphological processing including opening and closing of the head binary masks was performed. This single MR slice was subsequently

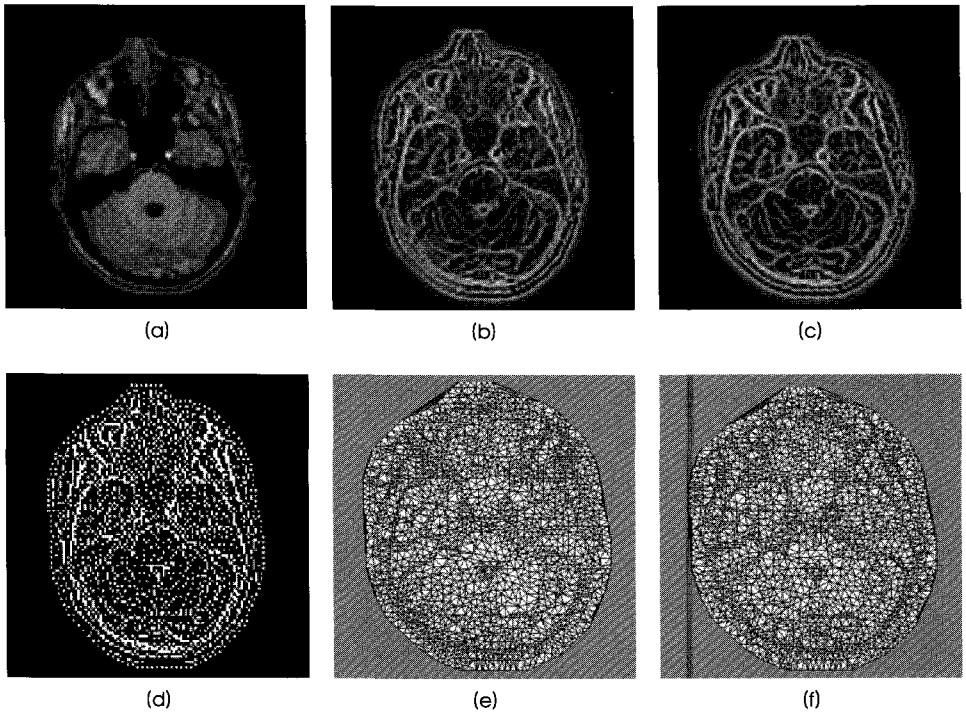

Fig. 1. Content-adaptive meshes of a MR image using the conventional method. (a) MR image, (b) feature map using f_{max}, (c) using f_{Hmax}, (d) content-adaptive nodes from (c), (e) Content-adaptive meshes from (b) with 2327 nodes and 4562 elements, and (f) cMeshes from (c) with 2326 nodes and 4560 elements

used in further processing of feature map extraction and cMesh generation.

B. cMesh Generation

Conventional cMesh Generation

Fig. 1 shows a set of results of 2-D conventional cMesh generation obtained by applying the techniques introduced by Yang *et al* to MR images. Fig. 1 (a) is a MR image, (b) conventional feature map obtained using f_{max}, (c) another suggested feature map using f_{Hmax}. Fig. 1 (d) shows content-adaptive nodes from Fig. 1 (c). Fig. 1 (e) and (f) show content-adaptive meshes in 2-D from Fig. 1 (b) and (c) respectively. There are 2327 nodes / 4562 triangular elements in Fig. 1 (e) and 2326 nodes / 4560 elements in Fig. 1 (f). The triangle with different sizes indicates adaptive characteristics of mesh generation in accordance with the two different feature maps. These meshes are compared to the cMeshes produced using the advanced feature map extractors in the subsequent sections.

Advanced cMesh generation

We have generated the cMeshes of the given MRI using the new and advanced feature maps. Figs. 2 (a), (b), and (c) display the feature maps obtained using f_{H+}, f_H, and f_{H-} derived from Hessian approach. Their corresponding cMeshes are shown in Fig. 2 (d), (e), and (f) respectively. In comparison to the results in Fig. 1, there are 2326 nodes / 4560 elements in Fig. 2 (d), 2324 nodes / 4556 elements in Fig. 2 (e), and 2329 nodes / 4566 elements in Fig. 2 (f). The high sensitivity of the Hessian tensor to the given MRI is clearly demonstrated inside image contents. These cMeshes are also evaluated in the following sections.

Fig. 3 shows a set of demonstrative results from the Structure tensor approach Figs. 3 (a), (b), and (c) show the proposed feature maps acquired using f_{S+}, f_S, and f_{S-} respectively. The corresponding cMeshs are described in Fig. 3 (d), (e), and (f). There are 2323 nodes / 4554 elements, 2325 nodes / 4558 elements, and 2323 nodes / 4554 elements respectively. Based on these results, it indicates that the Structure tensor-driven feature extractor yields optimal information on image features and their resultant cMeshes look most adaptive to the contents of given MRI. That is larger elements are present in the homogeneous regions and smaller elements in the high frequency regions with reasonable numbers of nodes and elements. Content-adaptive nature is clearly visible in the contents of the given MRI.

Also by using the Mean and Gaussian curvature, the feature maps obtained by f_M and f_G were generated as shown in Fig. 4 (a) and (b) respectively. The results of cMesh generation were described in Fig. 4 (c) and (d) as well. The characteristics of curvatures to the image features are clearly noticeable.

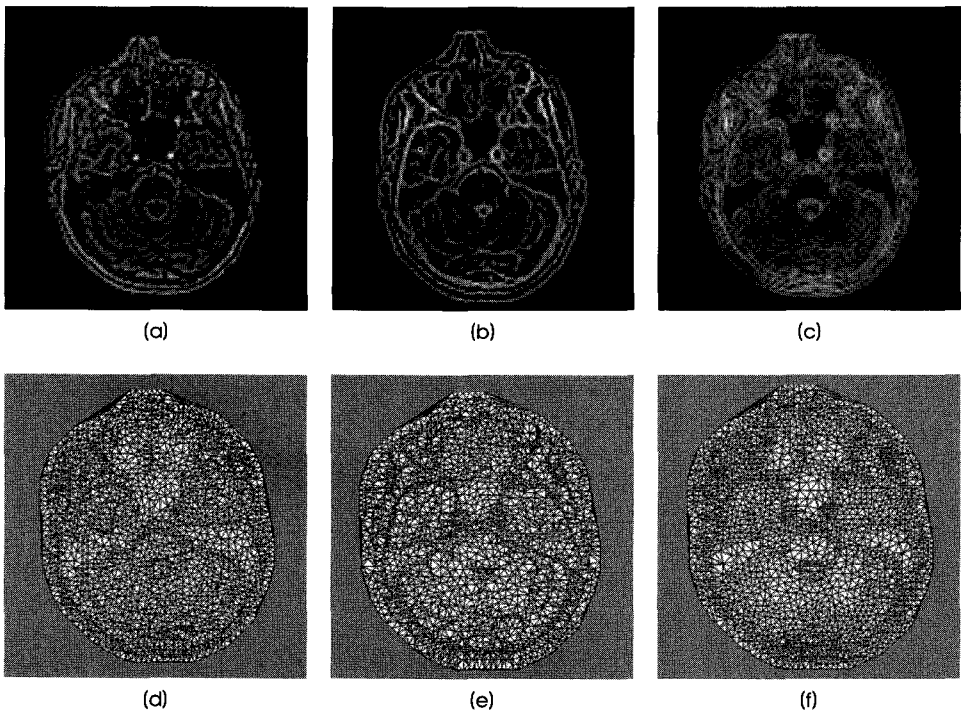

Fig. 2. Hessian tensor-driven feature extractor. (a) feature map using f_{H+}, (b) using f_H, (c) using f_{H-}, (d) cMeshes from (a) with 2326 nodes and 4560 elements, (e) from (b) with 2324 nodes and 4556 elements, (f) from (c) with 2329 nodes and 4566 elements

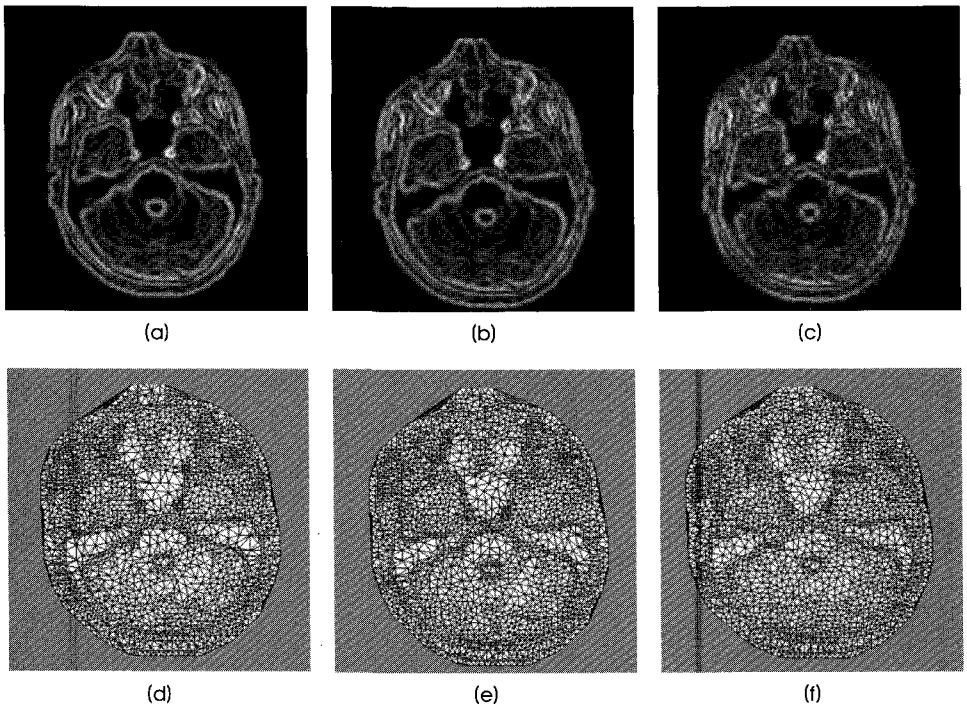

Fig. 3. Structure tensor-driven feature extractor. (a) feature map using f_{S+}, (b) using f_S, (c) using f_{S-}, (d) cMeshes from (a) with 2323 nodes and 4554 elements, (e) from (b) with 2325 nodes and 4558 elements, (f) from (c) with 2323 nodes and 4554 elements

Table 1. Numerical Evaluations of cMeshes

Method	No. of Nodes (Elements)	MR vs. Feature Map	MRI vs. Recon. MR		cMesh Quality		No. of Poor Elements :	k
		CC	RMSE	RE	Mean	Std.	q<0.6	
f_{max}	2327 (4562)	0.4474	40.1138	0.2104	0.7889	0.1591	503	2.5
f_{Hmax}	2326 (4560)	0.4945	46.9754	0.2464	0.7750	0.1622	617	2.565
f_{H+}	2326 (4560)	0.6751	34.9433	0.1833	0.7994	0.1543	418	1.45
f_H	2324 (4556)	0.4951	46.3831	0.2433	0.7757	0.1645	649	1.28
f_{H-}	2329 (4566)	0.6191	34.9433	0.1833	0.8194	0.1402	224	0.868
f_{S+}	2323 (4554)	0.6040	31.9609	0.1677	0.8115	0.1445	284	1.59
f_S	2325 (4558)	0.6072	31.9340	0.1675	0.8167	0.1418	243	1.565
f_{S-}	2323 (4554)	0.6053	32.9625	0.1729	0.8209	0.1438	254	1.62
f_M	2326 (4560)	0.6751	34.9433	0.1833	0.7994	0.1543	418	2.9
f_G	2325 (4558)	0.6982	28.9611	0.1414	0.8342	0.1348	166	4.71

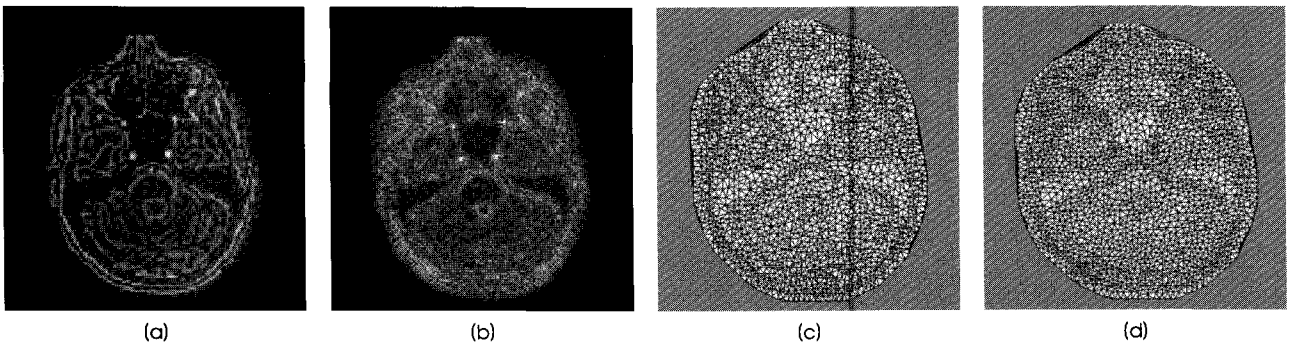

Fig. 4. Curvature-based feature extractor. (a) feature map using f_M, (b) using f_G, (c) cMeshes from (a) with 2326 nodes and 4560 elements, (d) from (b) with 2325 nodes and 4558 elements

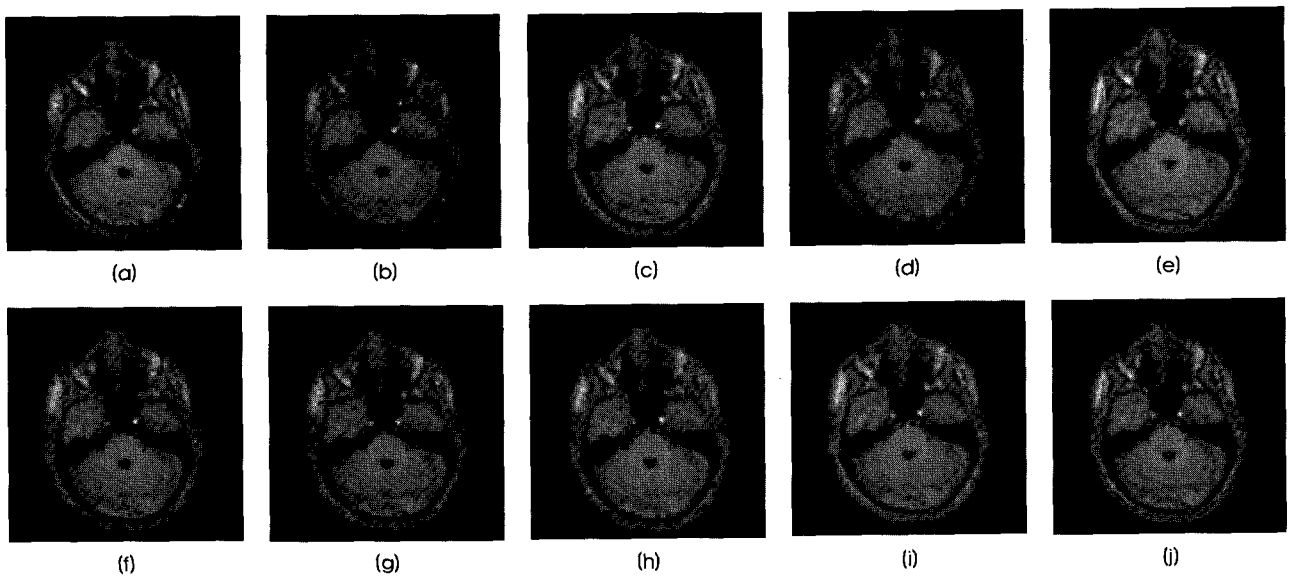

Fig. 5. Reconstructed MRI using the sampled nodal intensity values. (a) using the nodes from f_{max}, (b) f_{Hmax}, (c) f_{H+}, (d) f_{H}, (e) f_{H}, (f) f_{S+}, (g) f_{S}, (h) f_{S-}, (i) f_{M}, (j) f_{G} respectively

C. Numerical Evaluations of cMeshes

As described in the previous section, we have generated the reconstructed MRIs using its nodal intensity values for comparison of the content-adaptiveness of the cMeshes. Fig. 5 shows a set of reconstructed MRIs using conventional nodes from f_{max} and f_{Hmax}, proposed nodes derived from the eigenvalues of the Hessian and Structure tensor, and nodes from the Mean and Gaussian curvature, f_M and f_G, respectively. As summarized in Table 1, since the characteristics of the Gaussian curvature are highly sensitive to the image contents including unnecessary noise and artifacts, the Gaussian curvature-based feature extractor produces the lowest RMSE and RE values. Also, the Structure tensor-driven feature extractor seems to generate the most content-adaptive meshes with reasonable numbers and content-adaptive morphology with respect to number of nodes (or elements) and mesh morphology as shown in Fig. 3.

The CC values in Table 1 show strong correlation between the Structure tensor-driven feature map and MRI, indicating the Structure-driven feature extractor generates much better demonstrative features. Although CC value of Structure tensor-driven approach is lower than feature map by f_{H+}, f_{H-}, f_M, and f_G, it produced the much lower RMSE and RE values, indicating the reconstructed MRI is much closer to the original MRI.

In the case of evaluations of cMesh quality, the result by f_G describes the highest value. Also the Structure tensor approach

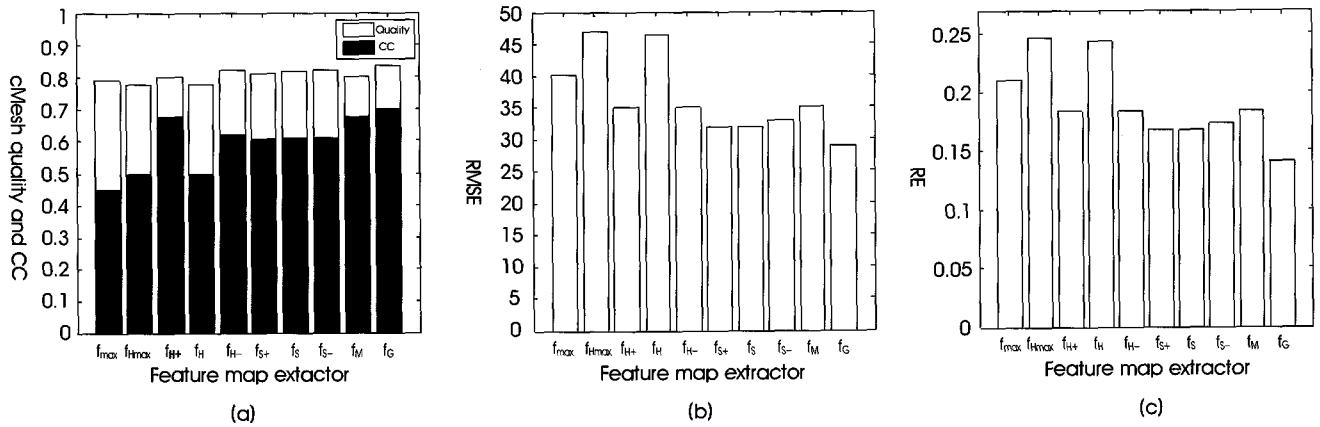

Fig. 6. Representative plots of numerical evaluation measure. (a) cMesh quality and CC between the feature map and the original MRI, (b) and (c) RMSE and RE between the reconstructed MRI and the original MRI respectively

show greatly acceptable values with the much lower number of poor elements compared to other feature map extractors, indicating the Structure tensor-driven approach can offer numerically accurate and efficient computational accuracy for FEA.

Fig. 6 shows the information in Table 1 in plots. The overall results of cMesh quality and CC are plotted in Fig. 6 (a) simultaneously. The comparison between MRI and the reconstructed MRI is also shown in Fig. 6 (b) and (c) in terms of RMSE and RE respectively.

Ⅳ. DISCUSSION

The advanced methodology to generate accurate and specific feature maps presented in this work offers more choices for improved cMesh generation. We believe that the cMesh generation schemes with more accurate and specific feature maps, thereby resulting in computation efficiency and accuracy on FEA, should be useful in studying bioelectromagnetic problems. As demonstrated on the presented methodology, we have tested various feature maps to generate cMeshes from a single MR slice, and then we have evaluated the effects on content-adaptiveness and the quality of cMesh triangle elements from each cMesh FE head model produced by specific feature map generation techniques, which could be used in forward and inverse computation of bioelectromagnetic source imaging of the brain [5, 6]. The numerical evaluations of cMesh FE head models were presented in terms of CC, RMSE, RE, and cMesh quality. The results demonstrate the Hessian tensor-driven feature extractor shows the less adaptive characteristic to contents of given MRI due to the high sensitivity to the contents including redundant content information and noises. However, the Structure tensor-driven feature extractor offers a significant effect on cMesh generation, since it shows much more adaptive behavior to the contents and quite acceptable mesh quality for FEA. Although we examined cMeshes applied by various feature maps, the methods for generating cMeshes related to more effective and efficient feature map extractors should be applicable to other fields of research as well.

One of the issues is to generate a patient-specific conducting model for the application of FEA in bioelectromagnetic problems or to produce deformable standardized meshes to represent complex domains [24]. With the advancements in measuring tissue properties [3, 6] which could be incorporated into the meshes, we believe in the subject-specific modeling approaches.

In the following work, we plan to investigate the numerical accuracy and compare the performance against the conventional meshes. Currently, we are investigating the accuracy of forward solutions of E/MEG source imaging and the effect of anisotropic conductivities within the content-adaptive FE models generated by the specific and improved feature maps against the conventional FE models. The presented techniques on advanced feature map extractors should also be applicable to other fields of bioelectromagnetic research areas.

Ⅴ. CONCLUSION

We have tested various feature maps for content-adaptive FE mesh generation and have evaluated the performance of the MRI content-adaptive FE head models generated through improved feature map extraction techniques. The Structure tensor-driven feature extractor seems to generate optimal information on image features and meshes are most adaptive to the contents of given MRI. The study described should be useful to the bioelectromagnetic imaging modalities such E/MEG source imaging [5, 6] and MREIT [3].

REFERENCES

[1] A. Samani, J, Bishop, M. J. Yaffe, and D. B. Plewes, "Biomechanical 3-D finite element modeling of the human breast using MRI data," *IEEE Trans. Med. Imaging.*, vol. 20, no. 4, pp. 271-279, 2001.

[2] N. K. Soni, K. D. Paulsen, H. Dehghani, and A. Hartov, "Finite element implementation of Maxwell's equations for image reconstruction in electrical impedance tomography," *IEEE Trans. Med. Imaging*, vol. 25, no. 1, pp. 55-61, 2006.

[3] E. Woo, S. Lee, T.-S. Kim, S. Oh, B. Lee, C. Park, J. Seo, S. Lee, and O. Kwon, "Conductivity and current density imaging of animal subject using MREIT technique," in *Proc. Int. Conf. Bioelectromagnetism and Int. Sym. Noninvasive Functional Source Imaging*, May, 2005.

[4] G. Martin, C. Guerin, S. Baillet, L. Garnero, and G. Meunier, "Influence of skull anisotropy for the forward and inverse problem in EEG: simulation studies using FEM on realistic head models," *Human Brain Mapping*, vol. 6, pp. 250-269, 1998.

[5] T.-S. Kim, Y. Zhou, S. Kim, and M. Singh, "EEG distributed source imaging with a realistic finite-element head model," *IEEE Trans. Nucl. Sci.*, vol. 49, no. 3, pp. 745-752, 2002.

[6] S. Kim, T.-S. Kim, Y. Zhou, and M. Singh, "Influence of conductivity tensors on the scalp electrical potential: study with 2-D finite element models," *IEEE Trans. Nucl. Sci.*, vol. 50, no. 1, pp. 133-138, 2003.

[7] U. Hartmann and F. Kruggel, "A fast algorithm for generating large tetrahedral 3D finite element meshes from magnetic resonance tomograms," in *Proc. IEEE Biomed. Image Analysis*, St. Barbara, 1998, pp. 184-192.

[8] Y. Yang, M. N. Wernick, and J. G. Brankov, "A fast approach for accurate content-adaptive mesh generation," *IEEE Trans. Image Processing*, vol. 12, no. 8, pp. 866-881, 2003.

[9] http://www.femlab.com

[10] http://www.nenastran.com

[11] Y. C. Zhang, S. A. Zhu, and B. He, "A second-order finite element algorithm for solving the three-dimensional EEG forward problem," *Phys. Med. Biol.*, vol. 49, pp. 2975-2987, 2004.

[12] M. Molinari, S. J. Cox, B. H. Blott, and G. J. Daniell, "Adaptive mesh refinement techniques for electrical impedance tomography," *Phys. Meas.*, vol., 22, pp.91-96, 2001.

[13] M. Ziolkowski and H. Brauer, "Methods of mesh generation for biomagnetic problems," *IEEE Trans. Magnetics*, vol. 32, no. 3, pp. 1345-1348, 1996.

[14] W. H. Lee, T.-S. Kim, M. H. Cho, and Y. B. Ahn, and S. Y. Lee, "Methods and evaluations of MRI content-adaptive finite element mesh generation for bioelectromagnetic problems," *Phys. Med. Biol.*, vol. 51, no. 23, pp. 6173-6186, 2006.

[15] K. A. Awada, D. R. Jackson, S. B. Baumann, J. T. Williams, D. R. Wilton, S. B. Baumann, and A. C. Papanicolaou, "Computational aspects of finite element modeling in EEG source localization," *IEEE Trans. Biomed. Engi.*, vol. 44, no. 8, pp. 736-752, 1997.

[16] Carmona R. A. and Zhong S., "Adaptive smoothing respecting feature directions," *IEEE Trans. Image Process.*, vol. 7, no. 3, pp 353-358, 1998.

[17] Khaled Z. Abd-Elmoniem, Abou-Bakr M. Youssef, and Yasser M. Kadah, "Real-time speckle reduction and coherence enhancement in ultrasound imaging via nonlinear anisotropic diffusion," *IEEE Trans. Biomed. Engi.*, vol. 49, no. 9, pp. 997-1014, 2002.

[18] Anthony Yezzi, Jr., "Modified curvature motion for image smoothing and enhancement," *IEEE Trans. Image Process.*, vol. 7, no. 3, pp 345-352, 1998.

[19] Gray, A. "The Gaussian and mean curvatures" and "Surfaces of constant Gaussian curvature," §16.5 and Ch. 21 in *Modern Differential Geometry of Curves and Surfaces with Mathematica, 2nd ed.* Boca Raton, FL: CRC Press, 1997, pp. 373-380 and 481-500.

[20] D. Tschumperle and R. Deriche, "Diffusion PDEs on vector-valued images," *IEEE Sig. Proc. Mag.*, Sep., pp. 16-25, 2002.

[21] Bank, Randolph E., *PLTMG: A software package for solving elliptic partial differential equations*, user's guide 6.0, Society for Industrial and Applied Mathematics, Philadelphia, PA, 1990.

[22] Mark D. and Dennis D. G., "Impact of mesh quality improvement systems in the accuracy of adaptive finite-element electromagnetic with tetrahedra," *IEEE Trans. Magnetics*, vol. 41, no. 5, pp 1692- 1695, 2005.

[23] J. R. Shewchuk, "What is a Good Linear Element?," in *Proc. 11th Int. Meshing Roundtable*, Albuquerque, NM, Sep. 2002, pp 115-126.

[24] A. P. Gibson, J. Riley, M. Schweiger, J. C. Hebden, S. R. Arridge, and D. T. Delpy, "A method for generating patient-specific finite element meshes for head modeling," *Phys. Med. Biol.*, vol. 48, pp. 481-485, 2003.